Point defect disorder in high-temperature solution grown Sr6Tb0.94Fe1.06(BO3)6 single crystals

Matias Velázquez, Stanislav Pechev, Mathieu Duttine, Alain Wattiaux, Christine Labrugère, Philippe Veber, Sonia Buffiere, Dominique Denux

Point defect disorder in high-temperature solution grown $Sr_6Tb_{0.94}Fe_{1.06}(BO_3)_6$ single crystals

M. Velázquez[1,*], S. Péchev[1], M. Duttine[1], A. Wattiaux[1], C. Labrugère[2], Ph. Veber[1,3], S. Buffière[1], D. Denux[1]

[1] ICMCB, UMR 5026 CNRS-Université de Bordeaux-Bordeaux INP, 87 avenue du Dr. A. Schweitzer, 33608 Pessac Cedex

[2] PLACAMAT, UMS 3626, CNRS-Université Bordeaux, 87 avenue du Dr. A. Schweitzer, 33600 Pessac, France

[3] Université Lyon, Université Claude Bernard Lyon 1, CNRS, Institut Lumière Matière UMR 5306, F-69100, Villeurbanne, France

* Corresponding author : ICMCB-CNRS UPR 9048, 87 Avenue du Docteur Albert Schweitzer, 33608 PESSAC Cedex. Tel. : +(33) 05 40 00 27 56, e-mail : matias.velazquez@icmcb.cnrs.fr

Abstract

New $Sr_6Tb_{0.94}Fe_{1.06}(BO_3)_6$ single crystals were obtained from lithium borate high-temperature solution growth under controlled atmosphere. Their average crystal structure was found to adopt the trigonal R-3 space group with lattice parameters a=12.2164 Å and c=9.1934 Å. A combined multiscale characterization approach, involving diffuse reflectance, X-ray photoelectron (XPS) and Mössbauer spectroscopies, was undertaken to establish the exact nature of the point defect disorder in this crystal structure. The $Fe_{Tb}^{\times}$ antisite disorder in the $Sr_6Tb_{0.94}Fe_{1.06}(BO_3)_6$ single crystals is different from the kind of point defect disorder known to exist in the powder phase material counterpart. The absence of Tb^{4+} cations in the crystal lattice was established by XPS, and that of any phase transition down to 4 K was checked by specific heat measurements. The magnetic susceptibility curve was found to follow a Curie-Weiss behaviour in the 4-354 K temperature range.

Keywords

High-temperature solution growth; Borate; Single crystal X-Ray Diffraction; Mössbauer spectroscopy; Tb compounds.

1. Introduction

In recent years, tremendous efforts have been dedicated to the search for and development of a significant number of Tb-based new crystals, essentially because of their potentially remarkable optical, magnetic and magneto-optic properties for the prospects of Faraday rotator [1-5], solid state lasers [6], phosphors [7-8], and biological cell imaging [9]. Tb^{3+} ions have been proved interesting for the Faraday rotation property which they induce in the visible and near infrared spectral range in such crystals as $Tb_5Ga_3O_{12}$ (TGG), or in Tb_2O_3 crystals recently grown for the first time [1]. In the latter crystal, the high Verdet constant (more than 3 times that of TGG crystals) in the visible and NIR spectral range cannot be explained by the increased Tb^{3+} concentration alone (twice as much as in TGG), and a detailed examination of the crystal field energy level structure and the Zeeman absorption effect in this compound is still lacking. In paramagnetic crystals down to very low temperatures, it is the combination of the Zeeman effect and crystal field splitting (4f elements) or spin-orbit splitting (3d-4d elements) that is at play. These simultaneous interactions modify the electronic energy level structure in such a way that the matrix elements of the electric dipole operator are different for left-handed polarized and right-handed polarized beams, and this difference between these matrix elements contribute to the Verdet constant. Another current interest in Tb-based crystals are new laser operations established in the visible spectral range. These new lasers can be pumped with frequency doubled InGaAs-based optically pumped semiconductor lasers (2ω-OPSL) between 475 and 490 nm [10], which deliver more than 5 W of output power and are commercially available. However, in such compounds as Tb^{3+}:YPO_4, due to the high energy position of the Tb^{3+} cations ground state ($^7F_6$) and the low energy position of the $4f^{n-1}5d^1$ configuration ground state, in the crystal bandgap [11], Tb^{3+} ions require low crystal field strength to minimize the propensity to excited-state absorption (ESA) of pump and/or laser light into 5d-states. Fortunately, the ESA from the $^5D_4$ state into the lowest 5d band multiplet is doubly spin-forbidden. Consequently, it is not surprising that in $LiLuF_4$ crystals, given the very high doping concentrations possible, pumping with a 2ω-OPSL at ~486 nm, laser operation was obtained at 540 nm (green, 300 mW with ~47-55% laser slopes and laser thresholds lower than 20 mW) and 588 nm (yellow, 82

mW with ~14% laser slopes and laser thresholds lower than 20 mW), despite the low absorption cross sections (~10^{-22} cm^2, 1-2 cm crystals are needed for one absorption length). Kraenkel *et al.* subsequently managed to obtain in a 2.1 cm-long Tb(28%):$LiLuF_4$ crystal, an impressive 1.125 W of green (542 nm) output power with a 52% laser slope and an output coupler of 1.6%. Finally, another major interest in finding new Tb-based materials is that of LED lighting [12-14].

In most of the optical applications, single crystals make it possible not only to determine their crystallographic structure but also to discover and exploit their intrinsic and anisotropic physical properties. They offer an opportunity to get rid of microstructural effects (diffusion at grain boundaries, pores, dislocations clouds, wall pinning by additional impurities or secondary phases, etc.) detrimental to the electromagnetic beam propagation and heat diffusion, establish crystalline birefringence-induced phase-matching conditions, as well as the polarization dependency of optically active species absorption and emission cross sections, concentrate the optically active (Tb) species (up to 10^{22} cm^{-3}) devoid of any translational degree of freedom, to increase laser gain or scintillation yield. In order to investigate the possibility of coupled optical and magnetic properties, since not too many compounds in this arena have been reported so far, we became motivated by combining Tb^{3+} with Fe^{3+} cations. In this research work, we intended to synthesize, grow and characterize a new Tb-based borate, namely $Sr_6TbFe(BO_3)_6$, and to investigate its crystallographic, as well as some optical and static magnetic properties, essentially from an experimental point of view (single crystal X-ray diffraction, powder diffuse reflectance, X-ray photoelectron –XPS– and Mössbauer spectroscopies, as well as specific heat and magnetic susceptibility measurements). The combined multiscale characterizations performed in this crystal established that the point defect disorder is different from the one of the powder materials counterparts known to date.

2. Materials and Methods

2.1. High-temperature solution growth

A first growth load was prepared from a mixture of $SrCO_3$ (8.85 g), Li_2CO_3 (4.43 g), H_3BO_3 (8.65 g), Tb_2O_3 (2.439 g) and Fe_2O_3 (1.06 g), dried overnight at 400 °C with a heating rate of 1 °C/mn. The Tb_2O_3 powder was prepared according to reference 1. The growth load volume decreased and it had a red colour. The mixture was then put in a Pt crucible, which in turn was placed in a vertical tubular furnace with controlled atmosphere. The furnace was heated at 1000

°C at a rate of 90 °C/h, kept at this temperature during 12 h, and then a slow cooling down to 500 °C at -1 °C/h was programmed, followed by a faster cooling down at room temperature at -60 °C/h. In order to simultaneously avoid Tb^{3+} oxidation and Fe^{3+} reduction, all the experiment was performed with a flow of 4N5 purity CO_2 gas at 2 bubbles/sec. The mass difference between the initial and the final Pt crucible content indicated that 74 % of the load was volatilized. Powder X-ray diffraction of the flux load indicated a complex mixture of $SrCO_3$, $P2_1/c$ $LiBO_2$ and $Sr_6TbFe(BO_3)_6$ phases. The total mass of the millimeter-sized yellow single crystals of $Sr_6TbFe(BO_3)_6$ we could extract from the bulk by means of slow dissolution in diluted and hot acetic acid was found to be 0.2572 g. A second growth run was performed by doubling the mass of initial charge and heating at 900 °C, all other parameters being unchanged. 55 % of the load volatilized and several yellow crystals could be extracted.

2.2. X-ray diffraction and crystal structure determination

Single crystal X-ray diffraction data were collected at room temperature on a Bruker Kappa APEX II diffractometer with sealed tube Mo radiation source. A crystal of suitable size was fixed with glue on the top of a glass rod. Indexing and data integration were performed using APEX2 [15]. Final data set was corrected for absorption using crystal faces' indexation and SADABS program [16]. Intrinsic phasing method and SHELXT program were used for crystal structure solution and the resulting model was refined with SHELXL least squares minimization [17]. Oelx2 [18] was used as working and editing results interface.

2.3. Specific heat, volumic mass, magnetic and Mössbauer spectroscopy measurements

Magnetic susceptibility was measured in the field cooling mode using a Quantum Design SQUID MPMS XL magnetometer operating in the 4.2−350 K temperature range under a 10 mT magnetic field. The four $Sr_6Tb_{0.94}Fe_{1.06}(BO_3)_6$ single crystals total mass was 49.4 mg. The sample was mounted in a capsule placed in a straw and the negligibly small (by at least two orders of magnitude in absolute magnetic moment) diamagnetic contribution of the capsule was not subtracted from our data. Specific heat measurements were made on two of the same crystals, of total mass 27.2 mg. The crystals were fixed on a sapphire sample holder with vacuum grease. The sample holder was mounted on the measurement shaft of a Quantum Design PPMS equipment interfaced to operate with a 2-τ pulse-step method corrected for the

grease baseline. The room temperature volumic mass used in the units conversion was that obtained from X-ray diffraction ρ_{XRD}=4.556 g.cm^{-3}. Ultrapycnometric measurements led to an experimental volumic mass of ρ_{exp}=(4.555±0.020) g.cm^{-3}.

^{57}Fe Mössbauer measurements were performed using a constant acceleration Halder-type spectrometer operating in transmission geometry with a room temperature ^{57}Co source (Rh matrix). A helium bath cryostat suitable for Mössbauer experiments was used in order to record spectra from room temperature down to 4.2 K. The velocity scale was calibrated according to the ^{57}Fe Mössbauer spectrum of a pure α-Fe^{0} foil recorded at room temperature. The polycrystalline absorbers were prepared in order to contain about 10 mg/cm^2 of iron and thus, to avoid saturation effects. The refinement of Mössbauer hyperfine parameters (δ isomer shift, Δ quadrupole splitting, Γ signal linewidth and relative areas) was performed using both homemade programs and the WinNormos software. Distributions of hyperfine parameters (quadrupole splitting) have been considered for overlapped components presenting apparent linewidth higher than 0.35 mm/s, following the method described by Hesse and Rübartsch [19].

2.4. Diffuse reflectance and XPS spectroscopies

The diffuse reflectance spectra of $Sr_6Tb_{0.94}Fe_{1.06}(BO_3)_6$ powder sieved down to 63 μm was measured from the near UV to the near IR spectral ranges (0.25-2.5 μm). Data acquisition was performed in a Cary 5000 spectrophotometer equipped with an integration sphere mounted in such a way as to avoid specular reflexion. The powder grain size distribution was investigated by SEM analysis: the average size of 876 grains was found to be d_{av}≈6.45 μm. A K-Alpha spectrometer (ThermoFisher Scientific) was used for surface analysis of the $Sr_6Tb_{0.94}Fe_{1.06}(BO_3)_6$ crystal and powders pressed onto indium foil. The monochromatized Al Kα source (hν=1486.6 eV) was activated with a spot size 200 μm in diameter as well as charge compensation. The full spectra (0-1350 eV) were acquired with a constant pass energy of 200 eV and high resolution spectra C1s, O1s, Tb3d and Tb4d, with a constant pass energy of 40 eV. We used F cubic Tb_4O_7 and Ia-3 cubic Tb_2O_3 powders as reference powder materials. The latter was obtained as in reference 1 by a thermal treatment at 1250 °C for 48 h under Ar/H_2 (5% vol.) of an initial minimum 5N purity powder supplied by Oximet Ltd, and the former was obtained by retreating the Tb_2O_3 powder at 1000 °C in air for 24 h. All powders were checked by X-ray diffraction and subsequent Le Bail fits to assess the crystal space group and lattice parameters.

3. Results

3.1. Crystal structure solution and description

The crystal structure of the borate was solved and refined within a trigonal symmetry model and R-3 space group. The starting structural model represented a perfectly stoichiometric $Sr_6TbFe(BO_3)_6$ compound. Here all cations were located in clearly identified and fully occupied crystallographic sites with a fairly good agreement factor R1 = 1.60 % at the end of the refinement. However, a careful analysis of the (Fo – Fc) difference Fourier maps showed significant electronic density excess of 1.8 eÅ^3 over the *3a* site of the Tb. The weighting scheme parameters were suggesting also some imperfections of the $Sr_6TbFe(BO_3)_6$ crystallographic model, especially with respect to some of the strong observed intensities which looked down-weighted. At this stage of the crystal structure refinement we benefited from additional hints coming from the complementary ^{57}Fe Mössbauer spectroscopy investigation which is discussed further in this work. The Mössbauer spectroscopy gave us two essential indications – only Fe^{3+} ions were present in our sample and all of them were distributed over two distinct crystallographic sites. In looking to the crystal structure model, besides its initial *3b* site, the iron could reasonably be relocated over the *3a* site of the Tb. Among the different possibilities of Fe statistical distribution over *3a* and *3b* sites, two models, very close to each other, stood out. In the first one, Fe^{3+} is partly substituted for Tb^{3+} on the *3a* site and the *3b* site stays fully occupied by Fe^{3+}. The resulting formula is $Sr_6Tb_{0.94}Fe_{1.06}(BO_3)_6$. In the second one, a partial Fe^{3+} for Tb^{3+} substitution over the *3a* site depletes the *3b* site, leaving on the latter some Fe^{3+} vacancies. In this case the formula could be written as $Sr_6(Tb_{0.94}Fe_{0.06})Fe_{0.94}(BO_3)_6$. It is immediately deduced that this cation distribution implies the presence of mixed valent Tb^{3+}/Tb^{4+} cations, so that the electric charge balance is insured. In order to clear out this question, an XPS analysis was undertaken, the result of which is displayed in Fig. 1.

3.2. X-ray photoelectron spectroscopy on $Sr_6Tb_{0.94}Fe_{1.06}(BO_3)_6$ single crystal and powder (obtained from our crushed single crystals)

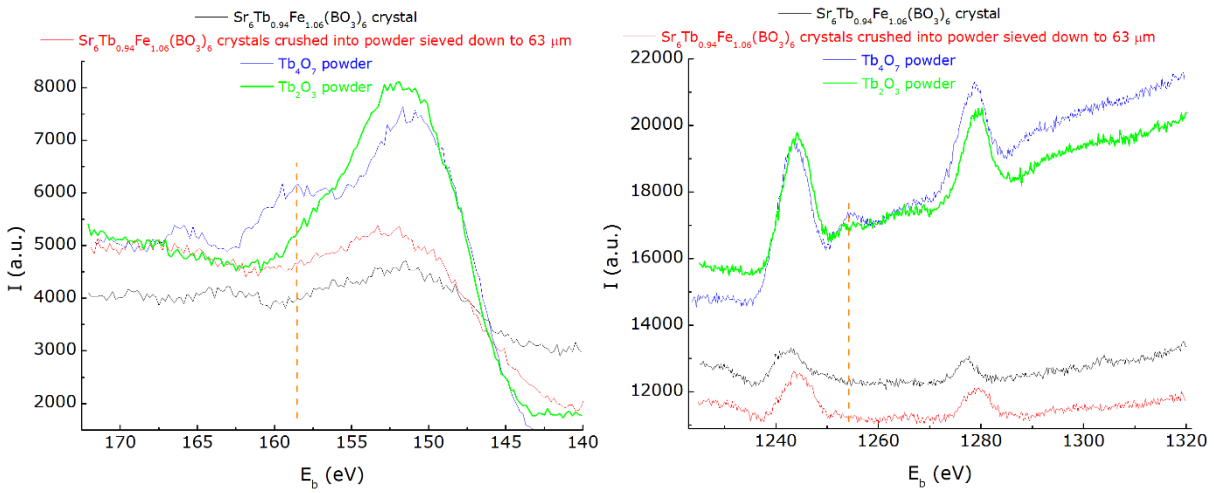

Figure 1. (a) Tb4d XPS spectrum, (b) Tb3d XPS spectrum of $Sr_6Tb_{0.94}Fe_{1.06}(BO_3)_6$, Tb_4O_7 and Tb_2O_3 powders. The dashed orange line is a guide to the eye.

In several Tb-based compounds [20-25], the presence of Tb^{4+} cations is evidenced by the occurrence of peaks at E_b's typically higher than 155 eV in the Tb4d spectra, and a $3d_{5/2}$ component at around ~1265 eV in the Tb3d spectrum. The Tb_2O_3 and Tb_4O_7 reference powders are interesting to compare because the former exhibits one single broad Tb4d peak centered around 151.6 eV, while the latter shows at least two (broad) peaks at 151.1 eV and 158.5 eV. We thus assign the broad peak around 158.5 eV to Tb^{4+} 4d states. The Tb4d spectra for both $Sr_6Tb_{0.94}Fe_{1.06}(BO_3)_6$ single crystal and 63-microns sieved powder (of crushed crystals from our growth experiments) obviously resemble the Tb_2O_3 powder one rather than the Tb_4O_7 one, with one broad peak centered around 151.5 eV (crystal) and 151.9 eV (powder). Hence, there are no Tb^{4+} cations detected in these samples. The Tb3d Tb_2O_3 and Tb_4O_7 reference powders spectra are quite similar through a $Tb3d_{5/2}$ peak at E_b=1244 eV and a $Tb3d_{3/2}$ peak at E_b=1279 eV with the exception of a small peak centered at E_b=1254.3 eV for the Tb_4O_7 powder, which we assign to Tb^{4+} cations. In the spectra of the single crystal or of the 63-microns sieved powder (of crushed crystals from our growth experiments) this smaller peak is not observed, which confirms the absence of Tb^{4+} in these samples. The possible presence of a small amount of Tb^{4+} cations in Tb_2O_3 powder sample, which could be evidenced by the small peak around 1254 eV, demonstrates that the XPS powder preparation is not reductive, and brings even more support to the contention that our $Sr_6Tb_{0.94}Fe_{1.06}(BO_3)_6$ single crystal and powder are devoid of Tb^{4+} cations, at least in the limit of detection of our technique.

3.3. Mössbauer spectroscopy on $Sr_6Tb_{0.94}Fe_{1.06}(BO_3)_6$ powder (obtained from our crushed single crystals)

As mentioned in section 3.1., the local environment of iron atoms was also investigated using ^{57}Fe Mössbauer spectroscopy. Two signals, labeled D1 and D2 in figure 2, were observed, which established the presence of two distinct crystallographic environments for Fe^{3+} cations. The signal is asymmetric and broad (Fig. 2). Further analyses at the magic angle (not shown here) confirmed that the apparent dissymmetry of the spectrum is not due to textural effect but is only the consequence of the occurrence of several Fe^{3+} signatures. The reconstruction of the room temperature spectrum of $Sr_6Tb_{0.94}Fe_{1.06}(BO_3)_6$ evidenced two components associated with two distinct iron sites. However, the peak width remains very high. Thus, the best fit to the experimental data was achieved by considering a distribution of the quadrupole splitting parameter for both signals (Table 1). Each signal was analyzed as the sum of quadrupole doublets with Lorentzian shape (line width 0.27 mm/s), isomer shift (0.40 mm/s for D1 and 0.34 mm/s for D2) deduced from the first calculation but with different quadrupole splitting values. Considering that Fe^{3+} is in a high-spin state and that the ^6S ground state has a spherically symmetric distribution of electronic charge, the quadrupole splitting arises mainly from the lattice contribution to the electronic field gradient (EFG) through the crystal field produced by ligands at the ^{57}Fe nucleus. Consequently, the observed quadrupole splitting distributions may reflect slight variations of the EFG due to different site distortions, some local cationic disorder (heterogeneous distribution of Sr^{2+}, Tb^{3+} and Fe^{3+} or occurrence of Tb^{3+} vacancies) and/or possible faults in the Tb- and Fe-octahedra stacking sequence. The main Mössbauer signal (D1, relative proportion about 70%) exhibits a broad distribution of the quadrupole splitting parameter (width of about 3 mm/s). Then, most of the iron sites appear to be influenced by this local disorder which may induce large distortions of the octahedral sites and thus a drastic change of the crystallographic site symmetry (loss of inversion center). On the other hand, the second signal (D2) is characterized by a narrower distribution and can be associated with slightly distorted octahedral sites. Moreover, D1 signal presents a higher value of isomer shift (0.40 mm/s) than D2 (0.34 mm/s), indicating that the Fe-O bonds have a more ionic character and then, the corresponding octahedral site may have more heterogeneous and larger Fe-O bond lengths.

At low temperature (4.2 K), no significant change was observed on the spectrum of $Sr_6Tb_{0.94}Fe_{1.06}(BO_3)_6$ (Figure 2) except an increase of the isomer shift values (+0.10 mm/s) due

to second-order Doppler effect arising from the difference of temperature between the sample and the gamma-emitting source (293 K). Thus, no magnetic ordering or structural transition was evidenced within the scanned temperature range (4.2–293 K) in good agreement with the results of the specific heat measurements and the magnetic properties of this compound (Figures 5 and 6). Moreover, a Mössbauer experiment performed at 4.2 K with a higher velocity scale (-12<*v*<+12 mm/s) (Figure S1) did not reveal the presence of any minor impurity phases (iron oxides for example) above the detection limit of this analytical method (about 1%).

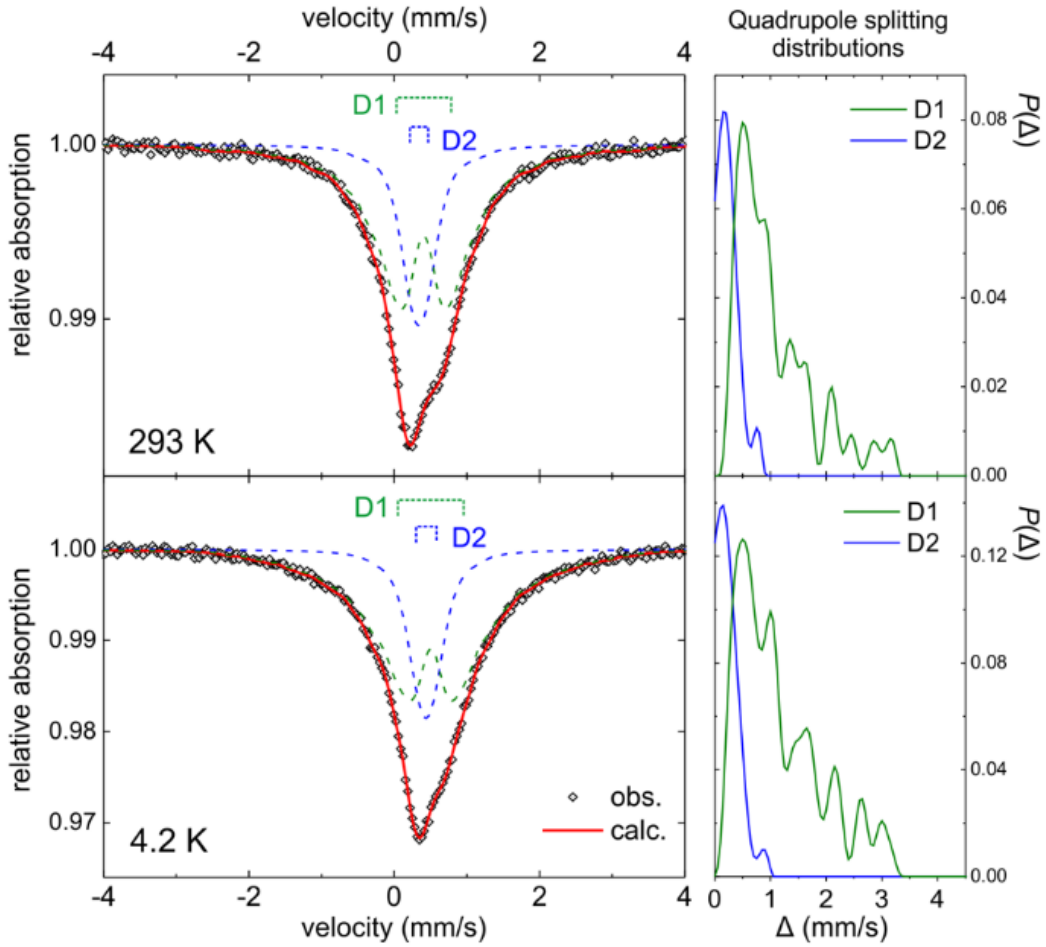

Figure 2. ^{57}Fe Mössbauer spectra of $Sr_6Tb_{0.94}Fe_{1.06}(BO_3)_6$ powder recorded at room temperature and 4.2 K. Each component (dashed lines) was calculated with a distribution of quadrupole doublets.

Table 1. ^{57}Fe Mössbauer hyperfine parameters of $Sr_6Tb_{0.94}Fe_{1.06}(BO_3)_6$. Δ*: value of Δ corresponding to the maximum of $P(\Delta)$; $w(\Delta)$: full width of quadrupole splitting distribution (see Figure 2).

Temperature	component	δ (mm/s)	Γ (mm/s)	Δ* (mm/s)	$w(\Delta)$ (mm/s)	%
293 K	D1	0.40(1)	0.27(-)	0.52	3.3	69(3)

	D2	0.34(1)	0.27(-)	0.17	0.9	31(3)
4.2 K	D1	0.51(1)	0.27(-)	0.52	3.4	71(3)
	D2	0.44(1)	0.27(-)	0.16	1.1	29(3)

Based on the observations coming from both Mössbauer and X-ray photoelectron spectroscopies, the final refinement of the crystal structure was performed considering a Tb^{3+}/Fe^{3+} disorder exclusively over the *3a* site which led to the formula $Sr_6Tb_{0.94}Fe_{1.06}(BO_3)_6$. The resulting agreement factor was improved to R1 = 1.39 %. The difference Fourier map peaks were flattened and the weighting scheme much more appropriate for a flat analysis of the intensities' variance. The X-ray diffraction data collection conditions and the structure refinement results are summarized in Table 2, and the atomic positions and site occupancies are gathered in Table 3.

Table 2. Crystal data and structure refinement for $Sr_6Tb_{0.94}Fe_{1.06}(BO_3)_6$.

Empirical formula	$B_6Fe_{1.06}O_{18}Sr_6Tb_{0.94}$
Formula weight	1087.14
Temperature/K	293.15
Crystal system	trigonal
Space group	R-3
a/Å	12.2164(2)
b/Å	12.2164(2)
c/Å	9.1943(2)
α/°	90
β/°	90
γ/°	120
Volume/$Å^3$	1188.33(5)
Z	3
$\rho_{calc}g/cm^3$	4.558
μ/mm^{-1}	25.215
F(000)	1472.0
Crystal size/mm	0.12 × 0.04 × 0.027
Radiation (Å)	MoKα (λ = 0.71073)
2Θ range for data collection/°	6.67 to 72.718
Index ranges	$-20 \leq h \leq 20$, $-20 \leq k \leq 20$, $-15 \leq l \leq 15$
Reflections collected	26564
Independent reflections	1292 [R_{int} = 0.0363, R_{sigma} = 0.0126]
Data/restraints/parameters	1292/0/52
Goodness-of-fit on F^2	1.101
Final R indexes [$I \geq 2\sigma$ (I)]	R_1 = 0.0139, wR_2 = 0.0288
Final R indexes [all data]	R_1 = 0.0175, wR_2 = 0.0294
Largest diff. peak/hole / e $Å^{-3}$	0.56(Sr) / -1.15(Fe2)

Table 3. Fractional atomic coordinates and equivalent isotropic displacement parameters ($Å^2×10^3$) for $Sr_6Tb_{0.94}Fe_{1.06}(BO_3)_6$. U_{eq} is defined as 1/3 of of the trace of the orthogonalized U_{IJ} tensor.

Wyckoff site letter	Occ	x	Y	z	U(eq)
3a	0.94	0	0	0	5.55(5)
3a	0.06	0	0	0	5.55(5)
3b	1	0.333333	0.666667	0.166667	6.19(9)
18f	1	0.23939(2)	0.37654(2)	0.2725(2)	7.56(4)
18f	1	0.17404(11)	0.55271(11)	0.5379(12)	9.17(19)
18f	1	0.12874(11)	0.16377(11)	0.15142(12)	9.18(19)
18f	1	0.40889(11)	0.33699(11)	0.14176(13)	10.9(2)
18f	1	0.52917(16)	0.39005(15)	0.9151(18)	7.0(2)

The $Sr_6Tb_{0.94}Fe_{1.06}(BO_3)_6$ crystallizes in the well-known $Sr_6HoSc(BO_3)_6$-type structure [26] where the Tb/Fe1 and Fe2 occupy two distinct regular octahedral sites and Sr is ninefold–coordinated. Alternated $Tb/Fe1O_6$ and $Fe2O_6$ octahedra are bridged by BO_3 groups, and then pile up to form columns along the *c* – axis, as drawn in Figure 3. Table 4 lists some selected bond lengths. The presence of cationic disorder over the octahedral sites is not something unusual with regards to other known isostructural compounds. In the parent $Sr_6HoSc(BO3)_6$ borate, an anti – site disorder of 8% between Ho *3a* and Sc *3b* sites has been reported [26]. In a recent work on the whole lanthanide $Sr_6LnFe(BO_3)_6$ family [27], it is reported a Ln – Sr disorder between Ln *3a* and Sr *18f* sites, based on a Rietveld refinement of powder diffraction data. Our single crystal diffraction data disagree with this model since when we tried to apply some Tb *3a* – Sr *18f* disorder our refinement diverged.

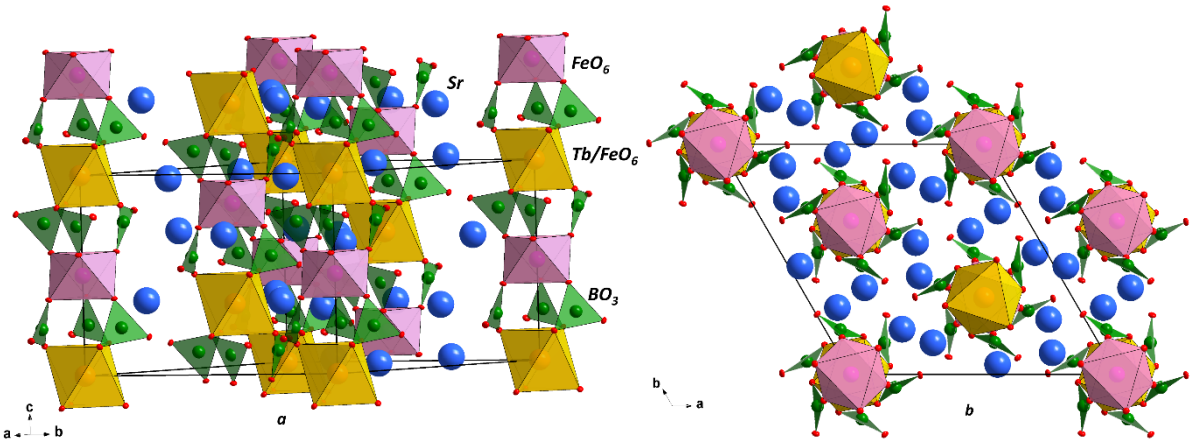

Figure 3. Three dimensional presentation (a) and projection along the *c*-axis (b) of the crystal structure of $Sr_6Tb_{0.94}Fe_{1.06}(BO_3)_6$.

Table 4. Bond lengths for $Sr_6Tb_{0.94}Fe_{1.06}(BO_3)_6$.

Atom	***Atom***	***Length/Å***	***Atom***	***Atom***	***Length/Å***
Tb/Fe1	O2	2.2952(11)	Sr	$O1^{12}$	2.7091(11)
Tb/Fe1	$O2^{1}$	2.2952(11)	Sr	$O1^{13}$	2.8032(12)
Tb/Fe1	$O2^{2}$	2.2952(11)	Sr	O1	2.6545(12)
Tb/Fe1	$O2^{3}$	2.2952(11)	Sr	$O2^{7}$	2.6385(12)
Tb/Fe1	$O2^{4}$	2.2952(11)	Sr	O2	2.5245(11)
Tb/Fe1	$O2^{5}$	2.2952(11)	Sr	$O3^{11}$	2.9161(12)
			Sr	$O3^{3}$	2.7506(12)
Fe2	$O1^{12}$	2.0231(11)	Sr	$O3^{7}$	2.5723(12)
Fe2	$O1^{15}$	2.0231(11)	Sr	O3	2.5750(12)
Fe2	$O1^{11}$	2.0231(11)			
Fe2	$O1^{16}$	2.0231(11)	B	$O1^{3}$	1.388(2)
Fe2	O1	2.0231(11)	B	$O2^{15}$	1.390(2)
Fe2	$O1^{13}$	2.0231(11)	B	O3	1.356(2)

[1]+Y-X,-X,+Z; [2]+Y,-X+Y,-Z; [3]-Y+X,+X,-Z; [4]-X,-Y,-Z; [5]-Y,+X-Y,+Z; [6]1/3-Y,-1/3+X-Y,-1/3+Z; [7]1/3+Y-X,2/3-X,-1/3+Z; [8]2/3-X,1/3-Y,1/3-Z; [9]-2/3+X,-1/3+Y,-1/3+Z; [10]-1/3-Y+X,-2/3+X,1/3-Z; [11]-1/3+Y,1/3-X+Y,1/3-Z; [12]2/3-Y+X,1/3+X,1/3-Z; [13]1-Y,1+X-Y,+Z; [14]1-X,1-Y,-Z; [15]+Y-X,1-X,+Z; [16]2/3-X,4/3-Y,1/3-Z

3.4. Diffuse reflectance measurements on $Sr_6Tb_{0.94}Fe_{1.06}(BO_3)_6$ powder (obtained from our crushed single crystals)

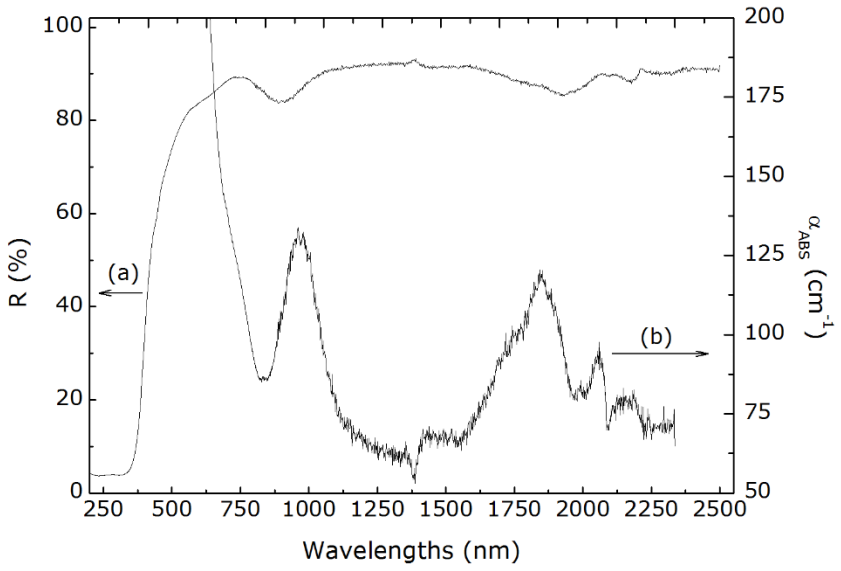

Figure 4. (a) Diffuse reflectance spectrum of $Sr_6Tb_{0.94}Fe_{1.06}(BO_3)_6$ powder (obtained from the crushed crystals grown by us) ; (b) the same spectrum transformed into absorption coefficient.

Assuming an average optical index n of 1.75, the reflectance spectrum was transformed into an "absorption coefficient-like" spectrum, according to $3/2 \times 1/(n^2 \times d_{av}) \times (1-R^2)/(1+R^2)$ (Figure 4 (b)). The resulting spectrum has one broad absorption peak centered around 900 nm and a number of broad and overlapping absorption peaks starting at 1.6 μm, the most intense of which being centered at 1924 nm. Taking into account the $Sr_6Tb_{0.94}Fe_{1.06}(BO_3)_6$ structure Fe^{3+} and Tb^{3+} cations concentrations ($[Fe^{3+}]=2.676\times10^{21}$ cm^{-3} ; $[Tb^{3+}]=2.373\times10^{21}$ cm^{-3}) leads to an order of magnitude $\sim2\times10^{-20}$ cm^2 for the near infrared absorption peak cross section, and $\sim(1-2)\times10^{-20}$ cm^2 cross section values for the middle infrared series of peaks. The first broad peak centered at 900 nm is likely to be due to Fe^{3+} $3d^5$ electrons intraconfigurational absorption transition, while the series of broad and overlapping peaks in the middle infrared range is due to Tb^{3+} cations 4f-4f electronic transitions. The order of magnitude estimated with our crude assumptions turns out to be rather high, much higher than what is found for instance in Tb_2O_3 for the middle infrared spectral range [1]. Indeed, according to the average $Sr_6Tb_{0.94}Fe_{1.06}(BO_3)_6$ crystal structure, the Fe^{3+} and Tb^{3+} cations are located on a crystallographic sites consisting of octahedra located in the *3a* and *3b* Wyckoff positions with point group symmetry -3, and so one does not expect the forced electric dipole mechanism to operate because of the presence of the inversion point symmetry. Even with an optical refractive index of 2, or with an average grain size 8 times higher than that measured, the absorption cross section peak value would still be in the range 10^{-21}-10^{-20} cm^2, a typical value of spin forbidden and forced electric dipole intraconfigurational transitions. This can only be explained by the fact that a great number –if not all– of Fe^{3+} and Tb^{3+} octahedra are so distorted by the $Fe^{\times}_{Tb}$ antisite disorder that the inversion point symmetry is locally removed while being conserved on average over large distances. Our analysis of the diffuse reflectance spectrum clearly confirms the disorder analysis made by Mössbauer spectroscopy. A tentative electronic gap was determined from the linear part of the Kubelka-Munk plots $(1-R)^2/2R$ *vs* energy, $E_g\approx3.16$ eV. The powder strongly absorbs below 458 nm, where the $\alpha_{ABS}\times d_{av}$ value become larger than 0.2, and so the use of Simmons' formulas to convert the spectra in absorption coefficient (α) units can only be seen as a rough approximation [28]. In any case, the crystals did not show any visible luminescence under 254 and 365 nm excitations at room temperature.

3.5. Static magnetic susceptibility and specific heat of the $Sr_6Tb_{0.94}Fe_{1.06}(BO_3)_6$ powder pellet

The temperature dependence of the MKSA magnetic susceptibility and its inverse, $\chi(T)$ and $\chi^{-1}(T)$, of four $Sr_6Tb_{0.94}Fe_{1.06}(BO_3)_6$ single crystals are shown in figure 5. No magnetic phase transition was observed down to 4 K, since a Curie-Weiss behaviour was obtained from 4 to 354.3 K with a Curie constant 0.84 K and a paramagnetic temperature -2.44 K. Assuming that the Curie constant results from two additive contributions, namely those arising from the Fe^{3+} and the Tb^{3+} cations, that the effective magnetic moment of the Fe^{3+} cations is exactly the one expected from theoretical free ion value ≈5.95 μ_B/Fe^{3+}, and taking the respective Fe^{3+} and Tb^{3+} cationic concentrations obtained from the XRD data, then the effective magnetic moment found for the Tb^{3+} cations roughly amounts to 9.76 μ_B/Tb^{3+}, a value that compares favorably to the theoretical free ion one 9.72 μ_B/Tb^{3+}. This is consistent with the absence of Tb^{4+} cations observed in the XPS spectra.

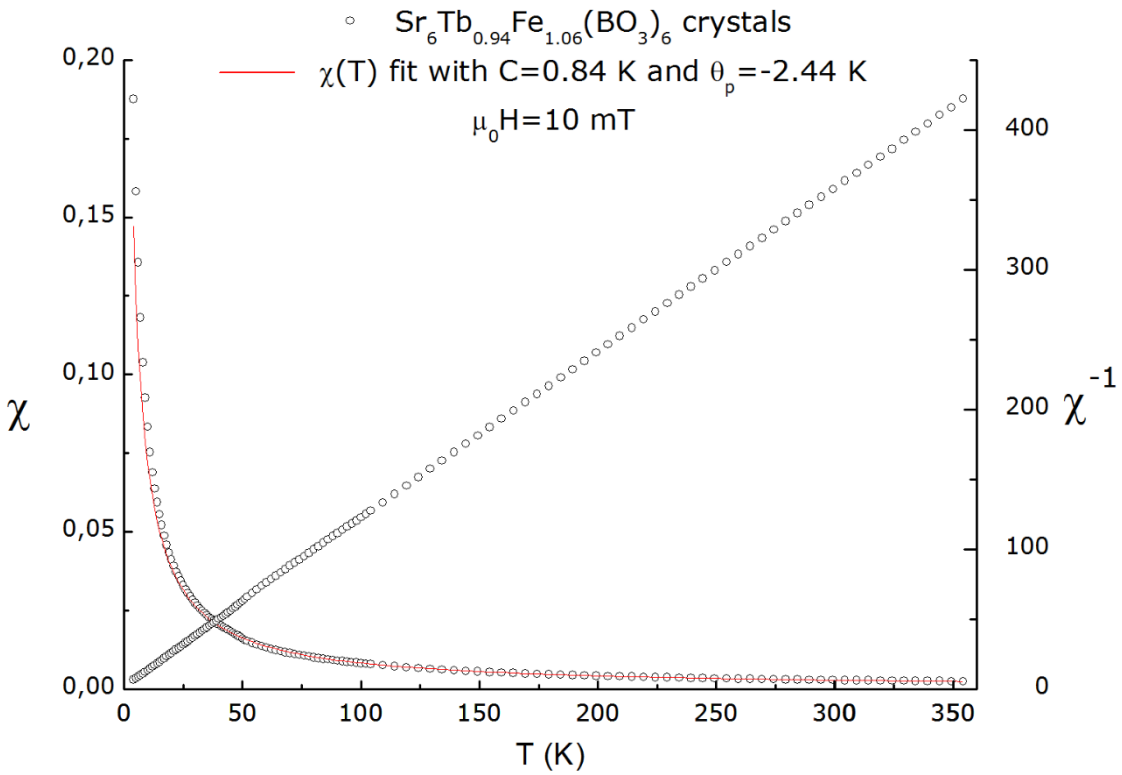

Figure 5. MKSA magnetic susceptibility and inverse magnetic susceptibility of $Sr_6Tb_{0.94}Fe_{1.06}(BO_3)_6$ single crystals.

In order to confirm the absence of any long range ordering down to 4 K, we performed the specific heat measurements that are plotted in figure 6. The specific heat data show the absence of any first and second order phase transition down to 4 K, consistently with the Mössbauer spectra recorded at room temperature and at 4.2 K (Fig. 2), and a much lower value than the Dulong & Petit limit of 96 R at room temperature. It can be looked upon as purely phononic in origin, at least in the range of temperatures higher than ~30 K. The phononic contribution could be approximated for temperatures higher than ~46 K by means of high-temperature series expansion (formula (5) of reference 29, and red curve in Figure 6), which yielded a high Debye temperature of ≈1159.8 K and the following Bernoulli numbers : B_1=-1.44022, B_2=1.70869, B_3=-1.23863. Such a value of the Debye temperature is higher than that of α-Al_2O_3 and $Li_6Eu(BO_3)_3$ [30].

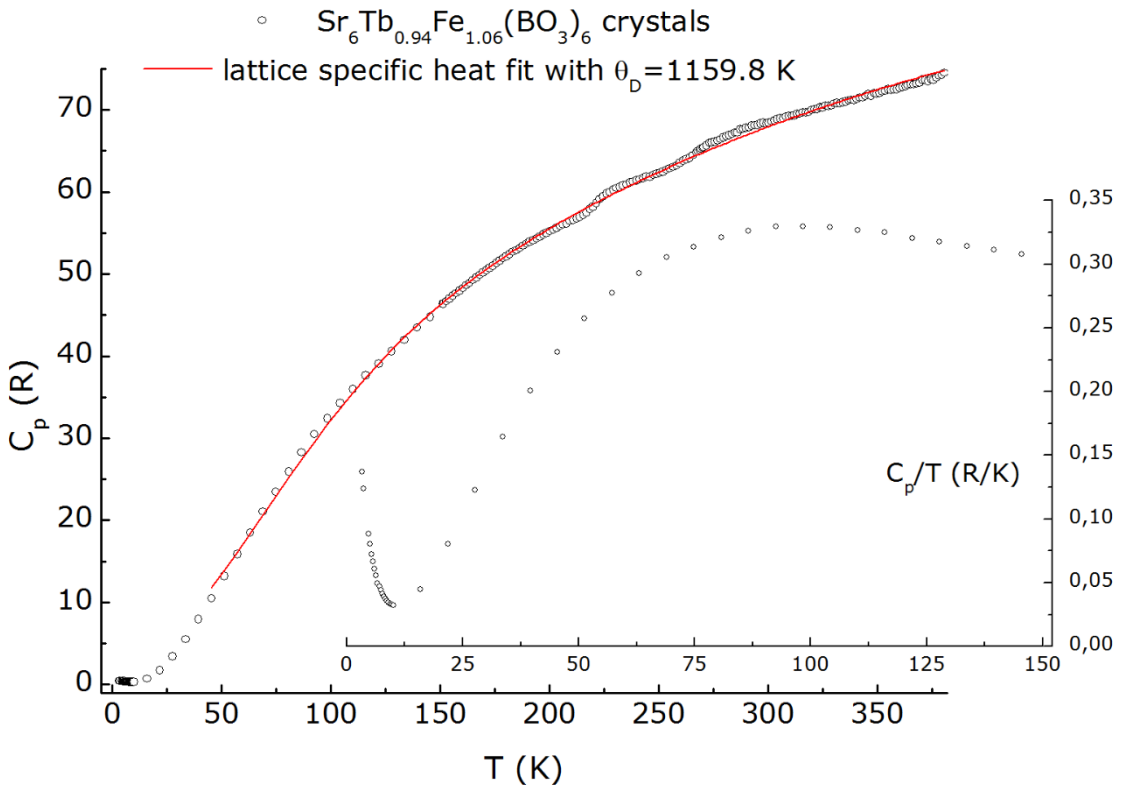

Figure 6. Temperature variation of a $Sr_6Tb_{0.94}Fe_{1.06}(BO_3)_6$ pellet. The inset shows a zoom at low temperature of the C_p/T function.

4. Discussion

X-ray diffraction, Mössbauer spectroscopy and optical spectroscopy are three techniques which can complementarily probe point defect disorder. While the first one leads to an average disorder over large distances, the second one is a middle range probe, and in the last one the intraconfigurational transitions are mainly determined by the point group of the specific Wyckoff position, that is, by the unit cell content. This explains why the Mössbauer and diffuse reflectance results seem to be at odds with the X-ray diffraction ones. This means that the average of the Fe^{3+} and Tb^{3+} octahedra distortions leads to an inversion point symmetry (*3a* and *3b* Wyckoff positions of the R-3 space group) which does not exist at the unit cell level of description. Such a situation is not rare. It is found for example in the $PbTiO_3$ compound the structure of which becomes centrosymmetric cubic under pressure, as determined by X-ray diffraction, but with Ti^{4+} cations deviated from the inversion point symmetry of their octahedra, as can be found by Raman spectroscopy or Ti-K edge XANES, a middle range probe and a local probe, respectively [31]. In our work, it is the Mössbauer spectroscopy that we used as a middle range probe (typically ~10 to 1000 unit cells) and the powder diffuse reflectance as a local probe to establish that the inversion point symmetry is locally removed by the overall cationic disorder. In the pioneer work of K. I. Schaffers *et al*. [26], it was found that in the M=Ho and M'=Sc compound of the same family, namely $Sr_6HoSc(BO_3)_6$, the $Ho_{Sc}^{\times}$-$Sc_{Ho}^{\times}$ antisite disorder amounted to some 8% and still the R-3 space group was kept for the X-ray single crystal data refinement. Another kind of point defect disorder was recently characterized in the M=Tb and M'=Fe compound, namely Sr_{Tb}'-$Tb_{Sr}^{\bullet}$ pairs in $(Sr_{6-x}Tb_x)Fe(Tb_{1-x}Sr_x)(BO_3)_6$ with x=0.4, which was obtained by solid state reaction [27]. Note that the powder analyzed in reference 27 was prepared with a 4% excess of H_3BO_3 and found to have a small amount of remaining $TbBO_3$ impurity phase. It turns out that the inverse magnetic susceptibility exhibits a slight curvature, from low to room temperature, the fitting of which required the introduction of some temperature-independent paramagnetism (TIP) contribution and led to an effective moment of the Tb^{3+} cations ~9.40 μ_B/Tb^{3+}. In addition, even with the introduction of a TIP component, the fit only holds for the 50-300 K temperature range. In our single crystals of composition $Sr_6Tb_{0.94}Fe_{1.06}(BO_3)_6$, the magnetic susceptibility data fit to a simple TIP-free Curie-Weiss model proved to hold over a 350 K-broad temperature range and led to an effective magnetic moment of the Tb^{3+} cations much closer to the free ion value than the one of the

powder sample. Moreover, the nature itself of the cationic disorder in our single crystals is different, which is likely to be due to the synthesis process. Here again, such a situation is not surprising. In the realm of laser [32,33], Faraday rotator [1] or scintillation materials [34], it has very often been found that the formation of point, and also extended, defects differs in single crystalline materials and in powder or ceramics materials. When a distribution of elements among non equivalent crystallographic sites is possible in a crystal structure, a selective elemental macropartition profile will occur in the single crystal or in the grains of the powder. This macropartition, at the most basic level of explanation, is dictated by some equilibrium partition coefficient which expresses the relative solubility of the elements in the crystalline state and in the liquid state from which it is grown, and in a given grain and its grain boundary in a powder, keeping in mind that there are as many equilibrium partition coefficients as there are non equivalent crystallographic sites. It is clear that the partition driving forces at play at a solidification interface (the most obvious one, but not exclusive, being the elastic strain energy stored in the crystal upon substitution/insertion) are different from those at play at a grain boundary (solute-crystal size and elastic moduli effects, grain boundary softness and elastic constants anisotropy from grain to grain due to their random orientation). In the former case, equilibria with the relevant liquid phases (the shear modulus of which are vanishingly small) will have to be taken into account. Overimposed to these equilibrium thermodynamics effects are coupled kinetic (heat and solute transports) and hydrodynamic effects in crystal growth from the melt, and solute-vacancy pairs transport due to vacancy concentration thermal gradient (∂[V]/∂T) in grain growth. Thus, depending on the point defects-based applications foreseen with the material, and their underlying physical properties, single crystals or ceramics will be preferred [32-34], and for a given shape of material, process parameters will have to be tuned (for instance, the use of a flux or a pure melt in crystal growth might induce different type of defects or modify their macropartition [32,33]).

5. Conclusions

$Sr_6Tb_{0.94}Fe_{1.06}(BO_3)_6$ single crystals were obtained by highly-concentrated, high-temperature Li- and B-based solution growth under CO_2 atmosphere. Single crystal XRD demonstrated that they adopt a trigonal crystal structure with the R-3 space group and lattice parameters a=12.2164 Å and c=9.1943 Å. XPS measurements firmly established the absence of Tb^{4+} cations in the crystal structure. Diffuse reflectance and Mössbauer spectra showed that the $Fe_{Tb}^{\times}$ antisite disorder is strong and leads to local and middle range distortions likely to remove the

inversion point symmetry of the R-3 space group *3a* and *3b* Wyckoff positions. This inversion point symmetry removal explains why the Fe^{3+} ($3d^5$) visible and Tb^{3+} ($4f^8$) middle infrared intraconfigurational optical absorption bands are intense. The crystals behave as Curie-Weiss paramagnets with an effective moment that arises from the contributions of Fe^{3+} and Tb^{3+} cations magnetic moments, very close to their free ion values, 5.95 μ_B/Fe^{3+} and 9.76 μ_B/Tb^{3+}, respectively. The specific heat data did not reveal any phase transition down to 4 K, and the fit to a high-temperature series expansion led to an estimate of the rather high Debye temperature.

Acknowledgments

Pengyun Chen contributed to the single crystals preparation, extraction and powder XRD characterizations under a Chinese Scholarship Council/University of Bordeaux fellowship.

References

[1] P. Veber, M. Velázquez, G. Gadret, D. Rytz, M. Peltz, R. Decourt, CrystEngComm, 17 (2015) 492.
[2] Pengyun Chen, R. K. Li, J. Alloys Comp., 622 (2015) 859.
[3] Pengyun Chen, Mingjun Xia, R. K. Li, New J. Chem., 39 (2015), 9389.
[4] K. Shimamura, T. Kito, E. Castel, A. Latynina, P. Molina, E. Víllora, M. Prakasam, P. Veber, J. Chaminade, A. Funaki, T. Hatanaka, K. Naoe, Cryst. Growth Des., 10 (2010) 3466.
[5] F. Guo, X. Chen, Z. Gong, X. Chen, Z. Xiang, B. Zhao, J. Chen, Optical Materials, 47 (2015) 543-547.
[6] Philip Werner Metz, Daniel-Timo Marzahl, Ahmad Majid, Christian Krankel, Gunter Huber, Laser Photonics Rev., 10 (2) (2016) 335–344.
[7] W. Di, X. Wang, B. Chen, X. Zhao, Chemistry Letters, 34 (4) (2005) 566-567.
[8] T. Oya, D. Nakauchi, G. Okada, N. Kawaguchi, T. Yanagida, Nuclear Instruments & Methods in Physics Research, Section A: Accelerators, Spectrometers, Detectors, and Associated Equipment, 866 (2017) 134-139.
[9] G. Sotiriou, D. Franco, D. Poulikakos, A. Ferrari, ACS Nano, 6 (2012) 3888.
[10] A. Richter, G. Huber *et al*., Electr. Lett., 41 (14) (2005) 794.
[11] P. Dorenbos, J. Lumin., 91 (2000) 155.
[12] J. Burgin, V. Jubera, H. Debéda, B. Glorieux, A. Garcia, C. Lucat, Journal Materials Science and Engineering B, 46 (2011) 2235-2241.

[13] Yang T. H., Chen C. Y., Chang Y. Y., Glorieux B., Peng Y. N., Chen H. X., Chung T. Y., Lee T. X., Sun C. C., IEEE Photonics Journal, 6 (4) (2014) 8400510.
[14] Ching-Cheng Sun, Yu-Yu Chang, Tsung-Hsun Yang, Te-Yuan Chung, Cheng-Chien Chen, Tsung-Xian Lee, Dun-Ru Li, Chun-Yan Lu, Zi-Yan Ting, Benoît Glorieux, Yi-Chun Chen, Kun-Yu Lai and Cheng-Yi Liu, Journal of Solid State Lighting, 1 (2014) 19.
[15] Bruker (2012). APEX2 (Version 2013.12). Bruker AXS Inc., Madison, Wisconsin, USA.
[16] L. Krause, R. Herbst-Irmer, G. M. Sheldrick, D. Stalke, J. Appl. Cryst., 48 (2015) 3-10.
[17] G. M. Sheldrick, Acta Cryst. A71 (2015) 3-8.
[18] O. V. Dolomanov, L. J. Bourhis, R. J. Gildea, J. A. K. Howard, H. Puschmann, J. Appl. Cryst., 42 (2009) 339-341.
[19] J. Hesse, A. Rübartsch, J. Phys. E. Sci. Instrum., 7 (1974) 526-532.
[20] Li Liping, Wei Quan, Liu Hongjian, Zheng Dafang, Su Wenhui, Gaoya Wuli Xuebao, 8 (3) (1994) 184-189.
[21] Song Yan; Liu Guixia, Wang Jinxian, Dong Xiangting, Yu Wensheng, Physical chemistry chemical physics : PCCP, 16 (29) (2014) 15139-15145.
[22] Song Yan, Liu Guixia, Dong Xiangting, Wang Jinxian, Yu Wensheng, Journal of Luminescence, 171 (2016) 124-130.
[23] Wu Ying, Shi Chunshan, Huaxue Xuebao, 54 (5) (1996) 468-474.
[24] Li Liping, Wei Quan, Wang Yifeng, Liu Hongjian, Huang Changlie, Wang Chulei, Li Fan, Su Wenhui, Gaodeng Xuexiao Huaxue Xuebao, 13 (2) (1992) 217-220.
[25] Masumoto Keiko, Kimura Chiharu, Aoki Hidemitsu, Sugino Takashi, Solid State Communications, 150 (29-30) (2010) 1396-1399.
[26] K. I. Schaffers, T. Alekel III, P. D. Thompson, J. R. Cox, D. A. Keszler, J. Am. Chem. Soc., 112 (1990) 7068-7069.
[27] H. Inoue, Y. Doi, Y. Hinatsu, J. Alloys Comp., 681 (2016) 115-119.
[28] E. L. Simmons, Appl. Opt., 14 (6) (1975) 1380-1386.
[29] J. E. Gordon, M. L. Tan, R. A. Fisher and N. E. Phillips, Sol. St. Comm., 69 (6) (1989) 625-629.
[30] M. Velázquez, Ph. Veber, M. Moutatouia, P. de Marcillac, A. Giuliani, P. Loaiza, D. Denux, R. Decourt, H. El Hafid, M. Laubenstein, S. Marnieros, C. Nones, V. Novati, E. Olivieri, D. V. Poda, A. S. Zolotarova, Solid State Sciences, 65 (2017), 41-51.
[31] N. Jaouen, A. C. Dhaussy, J.-P. Itié, A. Rogalev, S. Marinel, Y. Joly, Phys. Rev. B, 75 (2007) 224115/1-5.

[32] Ph. Veber, M. Velázquez, V. Jubera, S. Pechev, O. Viraphong, CrystEngComm, 13 (16) (2011) 5220-5225.
[33] M. Velázquez, Ph. Veber, G. Buşe, Y. Petit, Ph. Goldner, V. Jubera, D. Rytz, A. Jaffres, M. Peltz, V. Wesemann, P. Aschehough, G. Aka, Optical Materials, 39 (2015) 258-264.
[34] S. Arjoca, E. G. Víllora, D. Inomata, Y. Arai, Y. Cho, T. Sekiguchi, K. Shimamura, J. Ceram. Soc. Jap., 124 (5) (2016) 574-578.

Figure and table captions

Figure 1. (a) Tb4d XPS spectrum, (b) Tb3d XPS spectrum of $Sr_6Tb_{0.94}Fe_{1.06}(BO_3)_6$, Tb_4O_7 and Tb_2O_3 powders. The dashed orange line is a guide to the eye.

Figure 2. ^{57}Fe Mössbauer spectra of $Sr_6Tb_{0.94}Fe_{1.06}(BO_3)_6$ powder recorded at room temperature and 4.2 K. Each component (dashed lines) was calculated with a distribution of quadrupole doublets.

Figure 3. Three dimensional presentation (a) and projection along the *c*-axis (b) of the crystal structure of $Sr_6Tb_{0.94}Fe_{1.06}(BO_3)_6$.

Figure 4. (a) Diffuse reflectance spectrum of $Sr_6Tb_{0.94}Fe_{1.06}(BO_3)_6$ powder (obtained from the crushed crystals grown by us) ; (b) the same spectrum transformed into absorption coefficient.

Figure 5. MKSA magnetic susceptibility and inverse magnetic susceptibility of $Sr_6Tb_{0.94}Fe_{1.06}(BO_3)_6$ single crystals.

Figure 6. Temperature variation of a $Sr_6Tb_{0.94}Fe_{1.06}(BO_3)_6$ pellet. The inset shows a zoom at low temperature of the C_p/T function.

Table 1. ^{57}Fe Mössbauer hyperfine parameters of $Sr_6Tb_{0.94}Fe_{1.06}(BO_3)_6$. Δ^*: value of Δ corresponding to the maximum of $P(\Delta)$; $w(\Delta)$: full width of quadrupole splitting distribution.

Table 2. Crystal data and structure refinement for $Sr_6Tb_{0.94}Fe_{1.06}(BO_3)_6$.

Table 3. Fractional atomic coordinates and equivalent isotropic displacement parameters ($Å^2\times10^3$) for $Sr_6Tb_{0.94}Fe_{1.06}(BO_3)_6$. U_{eq} is defined as 1/3 of of the trace of the orthogonalized U_{IJ} tensor.

Table 4. Bond lengths for $Sr_6Tb_{0.94}Fe_{1.06}(BO_3)_6$.

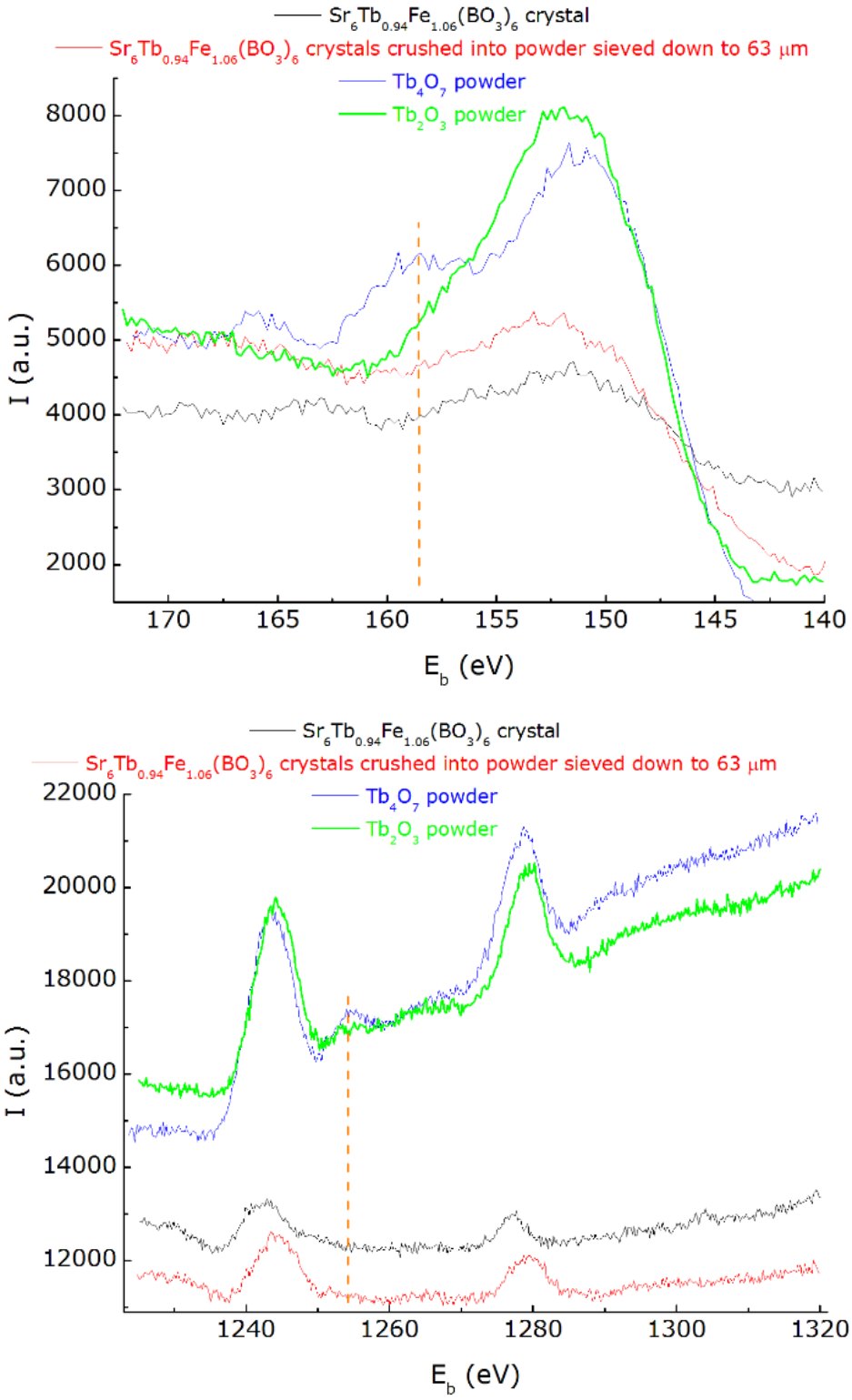
Sr6Tb0.94Fe1.06(BO3)6 crystal
Sr6Tb0.94Fe1.06(BO3)6 crystals crushed into powder sieved down to 63 μm
Tb4O7 powder
Tb2O3 powder
I (a.u.)
Eb (eV)
Sr6Tb0.94Fe1.06(BO3)6 crystal
Sr6Tb0.94Fe1.06(BO3)6 crystals crushed into powder sieved down to 63 μm
Tb4O7 powder
Tb2O3 powder
I (a.u.)
Eb (eV)

Figure 1

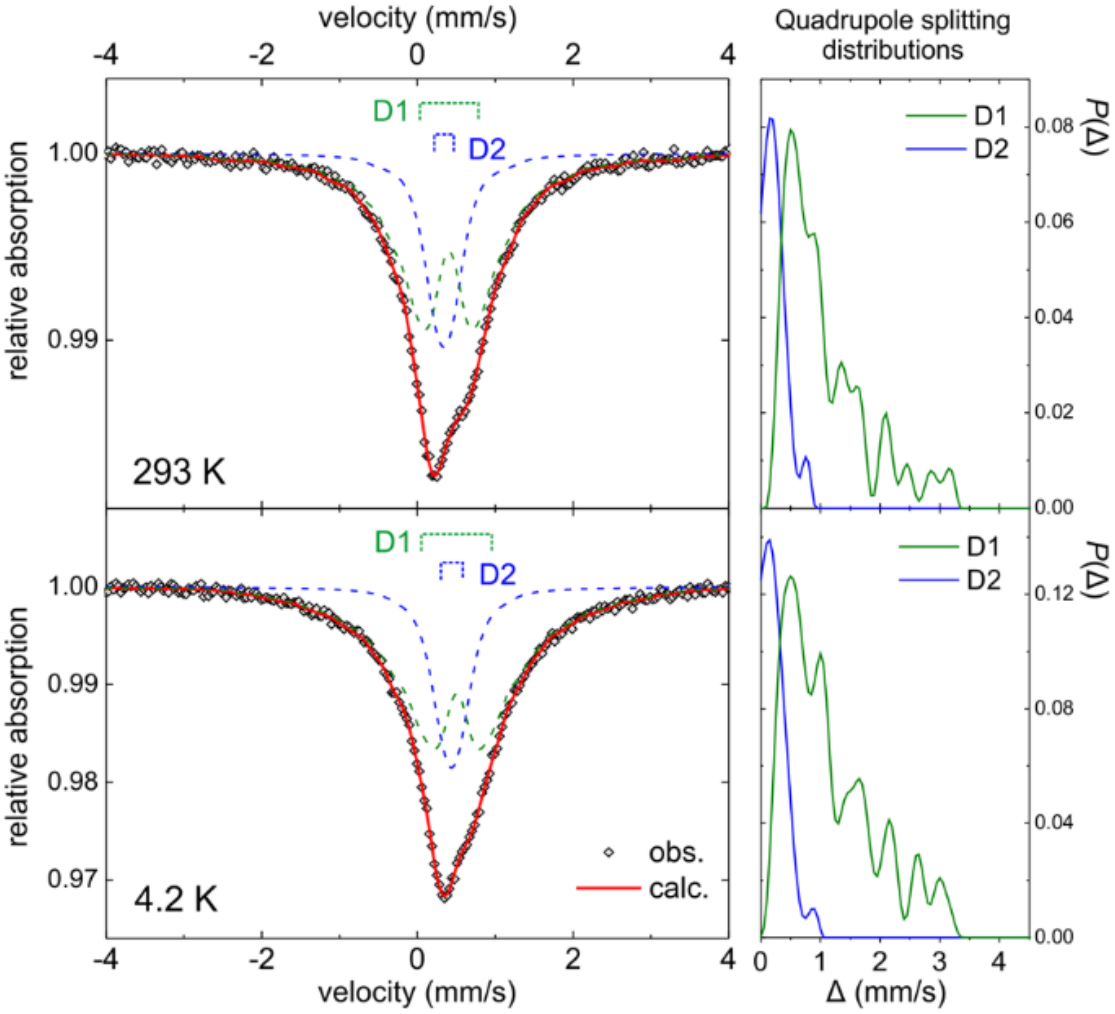
velocity (mm/s)
Quadrupole splitting distributions
relative absorption
D1
D2
293 K
4.2 K
obs.
calc.
P(Δ)
Δ (mm/s)

Figure 2

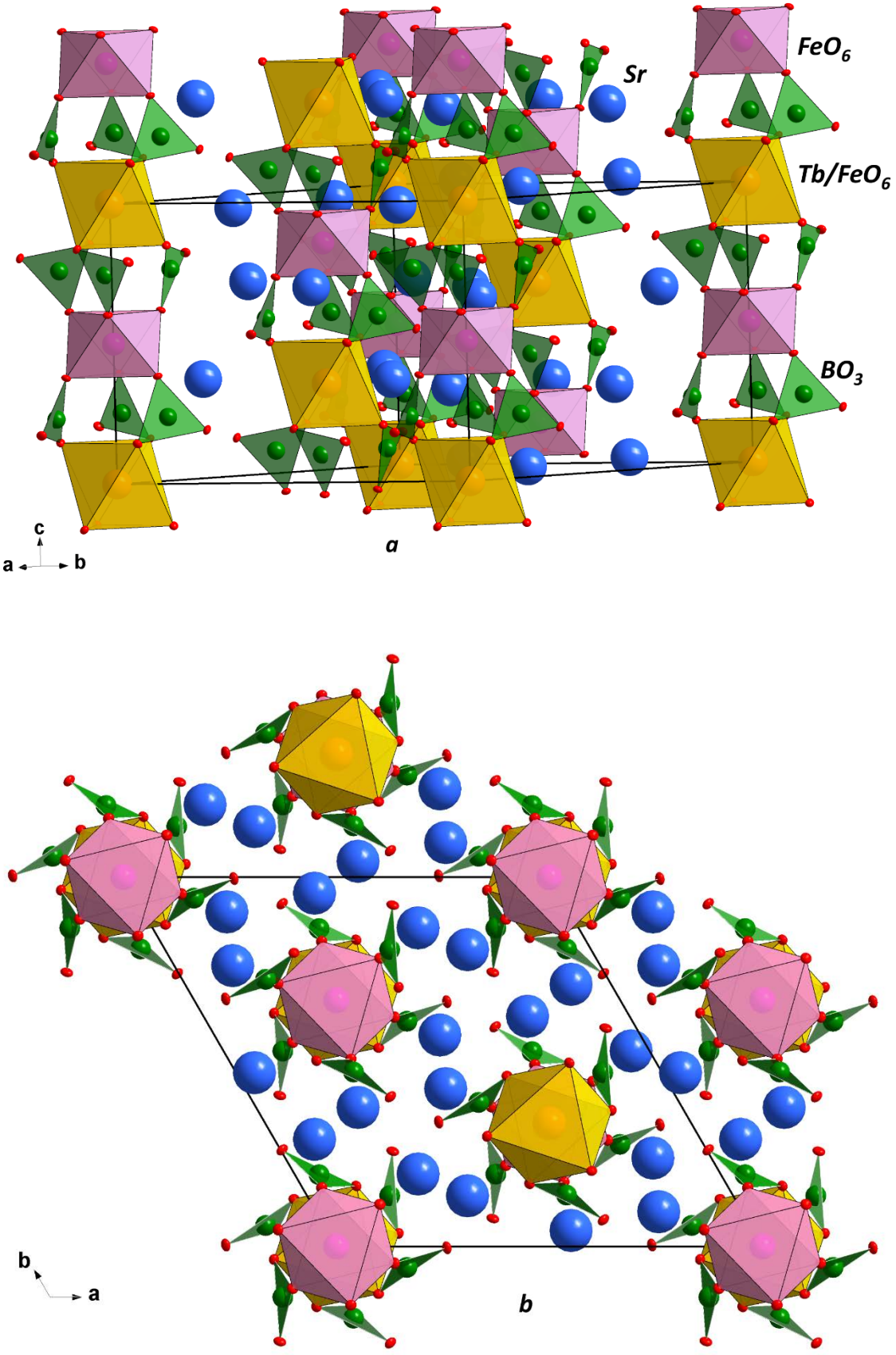

Figure 3

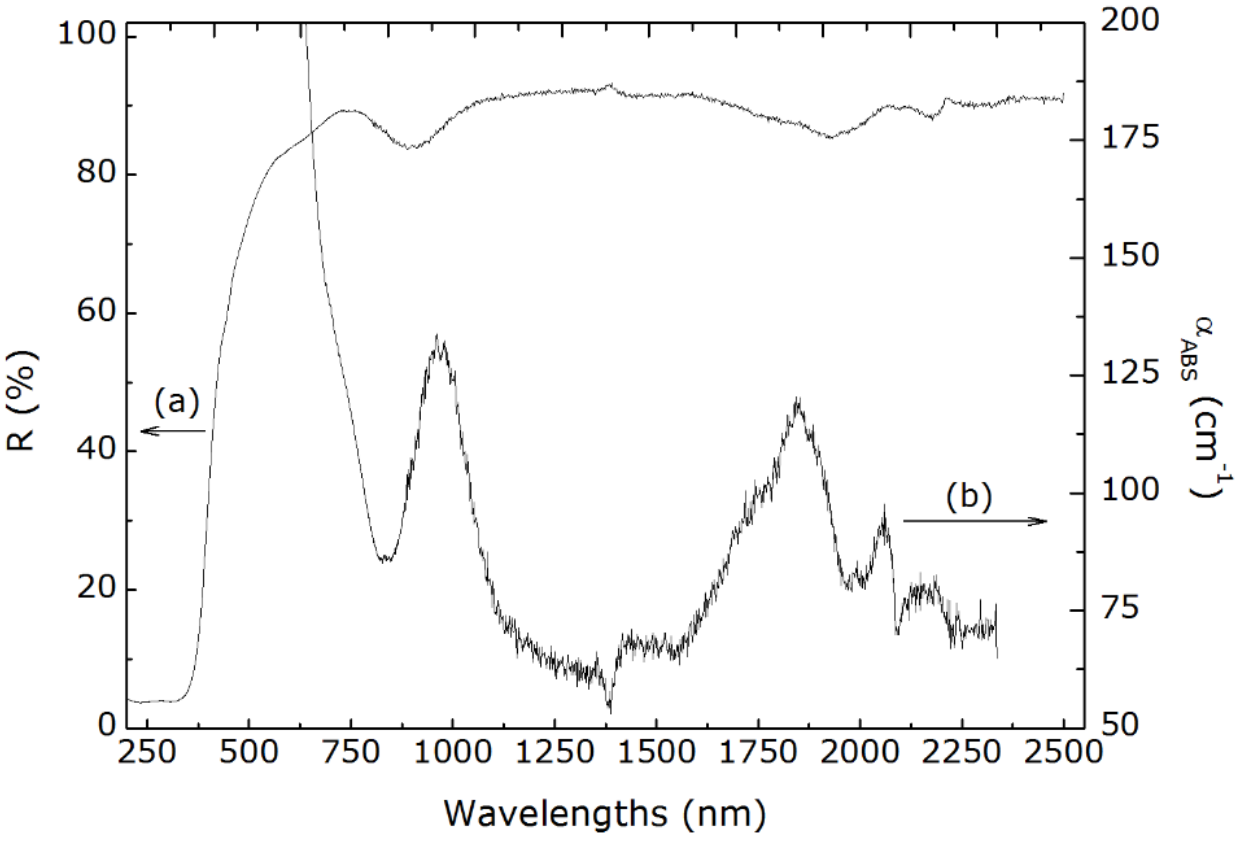
100
80
60
40
20
0
R (%)
(a)
200
175
150
125
100
75
50
α_{ABS} (cm^{-1})
(b)
250
500
750
1000
1250
1500
1750
2000
2250
2500
Wavelengths (nm)

Figure 4

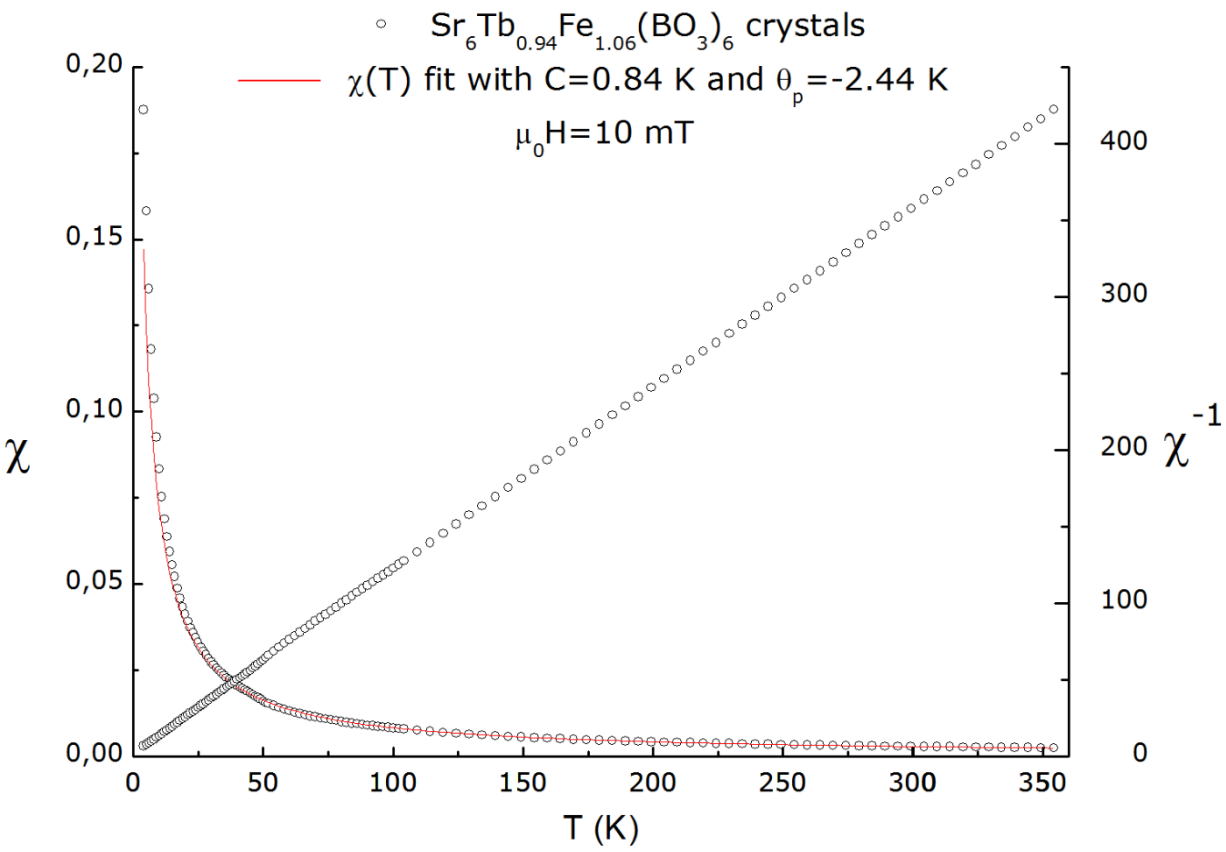
Sr6Tb0.94Fe1.06(BO3)6 crystals
χ(T) fit with C=0.84 K and θp=-2.44 K
μ0H=10 mT
χ
χ-1
T (K)
0,20
0,15
0,10
0,05
0,00
400
300
200
100
0
0
50
100
150
200
250
300
350

Figure 5

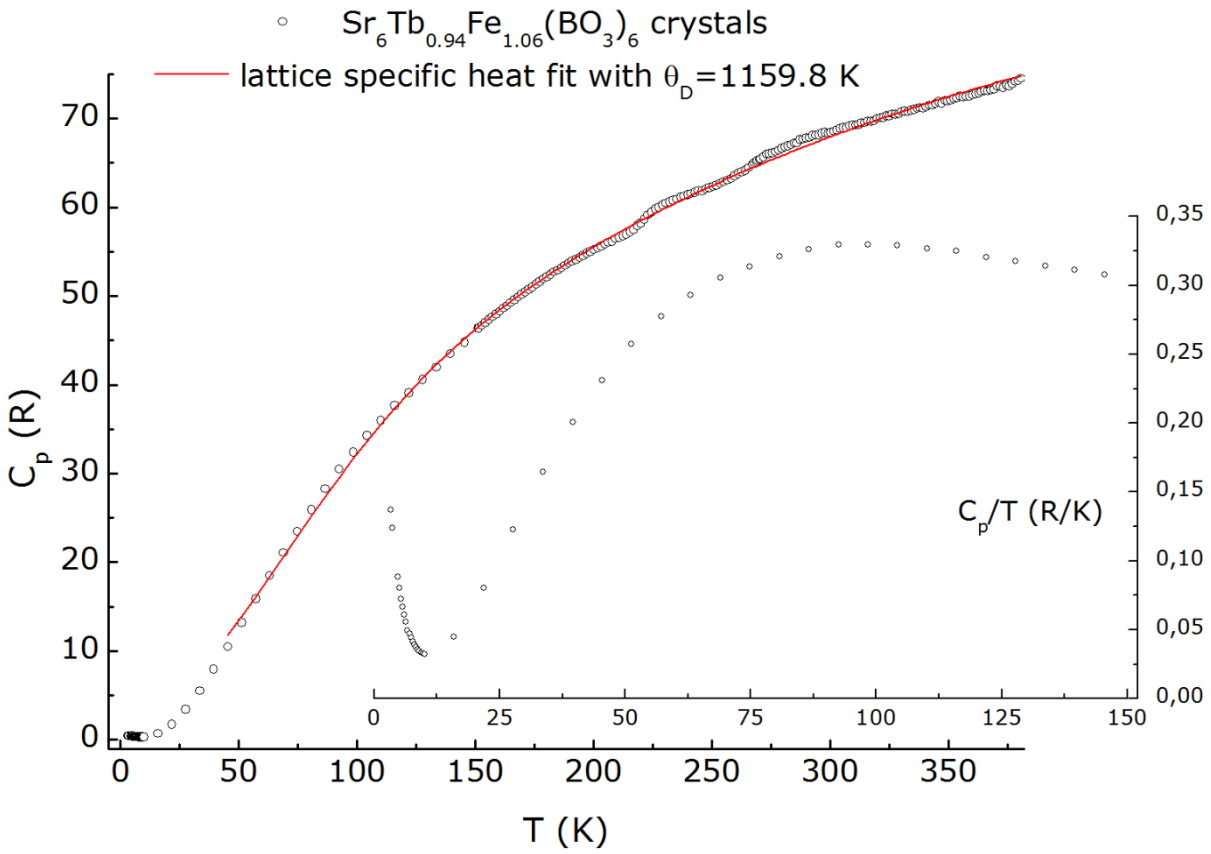
Sr6Tb0.94Fe1.06(BO3)6 crystals
lattice specific heat fit with θD=1159.8 K
Cp (R)
T (K)
Cp/T (R/K)
0
10
20
30
40
50
60
70
0
50
100
150
200
250
300
350
0,00
0,05
0,10
0,15
0,20
0,25
0,30
0,35
0
25
50
75
100
125
150

Figure 6

Table 1. ^{57}Fe Mössbauer hyperfine parameters of $Sr_6Tb_{0.94}Fe_{1.06}(BO_3)_6$. Δ*: value of Δ corresponding to the maximum of $P(\Delta)$; $w(\Delta)$: full width of quadrupole splitting distribution.

Temperature	component	δ (mm/s)	Γ (mm/s)	Δ* (mm/s)	$w(\Delta)$ (mm/s)	%
293 K	D1	0.40(1)	0.27(-)	0.52	3.3	69(3)
	D2	0.34(1)	0.27(-)	0.17	0.9	31(3)
4.2 K	D1	0.51(1)	0.27(-)	0.52	3.4	71(3)
	D2	0.44(1)	0.27(-)	0.16	1.1	29(3)

Table 2. Crystal data and structure refinement for $Sr_6Tb_{0.94}Fe_{1.06}(BO_3)_6$.

Empirical formula	$B_6Fe_{1.06}O_{18}Sr_6Tb_{0.94}$
Formula weight	1087.14
Temperature/K	293.15
Crystal system	trigonal
Space group	R-3
a/Å	12.2164(2)
b/Å	12.2164(2)
c/Å	9.1943(2)
α/°	90
β/°	90
γ/°	120
Volume/Å^3	1188.33(5)
Z	3
ρ_{calc}g/cm^3	4.558
μ/mm^{-1}	25.215
F(000)	1472.0
Crystal size/mm	0.12 × 0.04 × 0.027
Radiation (Å)	MoKα (λ = 0.71073)
2Θ range for data collection/°	6.67 to 72.718
Index ranges	$-20 \leq h \leq 20$, $-20 \leq k \leq 20$, $-15 \leq l \leq 15$
Reflections collected	26564
Independent reflections	1292 [R_{int} = 0.0363, R_{sigma} = 0.0126]
Data/restraints/parameters	1292/0/52
Goodness-of-fit on F^2	1.101
Final R indexes [$I \geq 2\sigma(I)$]	R_1 = 0.0139, wR_2 = 0.0288
Final R indexes [all data]	R_1 = 0.0175, wR_2 = 0.0294
Largest diff. peak/hole / e Å^{-3}	0.56(Sr) / -1.15(Fe2)

Table 3. Fractional atomic coordinates and equivalent isotropic displacement parameters ($Å^2×10^3$) for $Sr_6Tb_{0.94}Fe_{1.06}(BO_3)_6$. U_{eq} is defined as 1/3 of of the trace of the orthogonalized U_{IJ} tensor.

Atom	Wyckoff site letter	Occ	x	Y	z	U(eq)
Tb	*3a*	0.94	0	0	0	5.55(5)
Fe1	*3a*	0.06	0	0	0	5.55(5)
Fe2	*3b*	1	0.333333	0.666667	0.166667	6.19(9)
Sr	*18f*	1	0.23939(2)	0.37654(2)	0.2725(2)	7.56(4)
O1	*18f*	1	0.17404(11)	0.55271(11)	0.5379(12)	9.17(19)
O2	*18f*	1	0.12874(11)	0.16377(11)	0.15142(12)	9.18(19)
O3	*18f*	1	0.40889(11)	0.33699(11)	0.14176(13)	10.9(2)
B	*18f*	1	0.52917(16)	0.39005(15)	0.9151(18)	7.0(2)

Table 4. Bond lengths for $Sr_6Tb_{0.94}Fe_{1.06}(BO_3)_6$.

Atom	*Atom*	*Length/Å*	*Atom*	*Atom*	*Length/Å*
Tb/Fe1	O2	2.2952(11)	Sr	$O1^{12}$	2.7091(11)
Tb/Fe1	$O2^{1}$	2.2952(11)	Sr	$O1^{13}$	2.8032(12)
Tb/Fe1	$O2^{2}$	2.2952(11)	Sr	O1	2.6545(12)
Tb/Fe1	$O2^{3}$	2.2952(11)	Sr	$O2^{7}$	2.6385(12)
Tb/Fe1	$O2^{4}$	2.2952(11)	Sr	O2	2.5245(11)
Tb/Fe1	$O2^{5}$	2.2952(11)	Sr	$O3^{11}$	2.9161(12)
			Sr	$O3^{3}$	2.7506(12)
Fe2	$O1^{12}$	2.0231(11)	Sr	$O3^{7}$	2.5723(12)
Fe2	$O1^{15}$	2.0231(11)	Sr	O3	2.5750(12)
Fe2	$O1^{11}$	2.0231(11)			
Fe2	$O1^{16}$	2.0231(11)	B	$O1^{3}$	1.388(2)
Fe2	O1	2.0231(11)	B	$O2^{15}$	1.390(2)
Fe2	$O1^{13}$	2.0231(11)	B	O3	1.356(2)

[1]+Y-X,-X,+Z; [2]+Y,-X+Y,-Z; [3]-Y+X,+X,-Z; [4]-X,-Y,-Z; [5]-Y,+X-Y,+Z; [6]1/3-Y,-1/3+X-Y,-1/3+Z; [7]1/3+Y-X,2/3-X,-1/3+Z; [8]2/3-X,1/3-Y,1/3-Z; [9]-2/3+X,-1/3+Y,-1/3+Z; [10]-1/3-Y+X,-2/3+X,1/3-Z; [11]-1/3+Y,1/3-X+Y,1/3-Z; [12]2/3-Y+X,1/3+X,1/3-Z; [13]1-Y,1+X-Y,+Z; [14]1-X,1-Y,-Z; [15]+Y-X,1-X,+Z; [16]2/3-X,4/3-Y,1/3-Z